Contents lists available at ScienceDirect

Nuclear Inst. and Methods in Physics Research, A

journal homepage: www.elsevier.com/locate/nima

Full Length Article

Capability demonstration of a 3D CdZnTe detector on a high-altitude balloon flight

Sara Abraham [a,b,*], Yuefeng Zhu [a], Suzanne Nowicki [b], Peter Bloser [b], James Berry [a], Benigno Sandoval [b], Sara Lanctot [b], Matthew Petryk [a], Jonathan Deming [b], Alexei Klimenko [b], Zhong He [a]

[a] University of Michigan, 2355 Bonisteel Blvd, Ann Arbor, MI 48109, USA
[b] Los Alamos National Laboratory, Los Alamos, NM 87545, USA

ARTICLE INFO

ABSTRACT

In collaboration between the University of Michigan and Los Alamos National Laboratory, a 3D position-sensing CdZnTe (CZT) detector prototype was built and integrated into a high-altitude balloon platform to evaluate its performance in a space-like mixed-radiation environment. The detector prototype, Orion Eagle, was designed to operate in near-vacuum environments without any temperature regulation. Orion Eagle was hand-launched from NASA's Columbia Scientific Balloon Facility (CSBF) at Fort Sumner, NM on September 26, 2021, and successfully operated throughout a 9-hour flight, which reached 38.5 km in altitude. The flight met its objectives, successfully detecting atmospheric gamma rays and galactic cosmic rays, and raising the Technical Readiness Level from 4 to 6 for large-volume 3D CZT detector technology for space applications. Ionization tracks produced by charged particles create spatial signatures in the detector that are distinguishable from discrete gamma-ray interactions. Therefore, the 3D position-sensing capabilities using pixelated electrodes on a CZT detector can help enable discrimination of background charged particles from gamma-ray events without an anticoincidence shield. The potential for background rejection capability, ambient-temperature operation, gamma-ray coded-aperture and Compton imaging, and near High Purity Germanium (HPGe) energy resolution motivate the use of large-volume 3D CZT imaging spectrometers in future space missions.

1. Introduction

Gamma-ray spectrometers are regularly used in planetary science to probe the subsurface elemental composition of planetary bodies such as the Moon [1], Mars [2], Mercury [3], Venus [4], and asteroids Eros [5], Vesta and Ceres [6,7]. Gamma rays emitted from planetary materials provide key information on the subsurface elemental composition that can be paired with mineralogical data to help understand the formation and evolution of the planetary body. These gamma rays are the result of both radioactive decay and interactions between the subsurface materials and an activation source (i.e. galactic cosmic rays or a pulsed neutron generator). Currently, the spatial resolution of mineralogical data such as data acquired by infra-red spectroscopy, X-ray diffraction and many other methods, is usually better than that achieved with gamma-ray spectrometers. The diameter of a spatial resolution element with the Mars Odyssey Gamma Ray Spectrometer (GRS) on the Martian surface is about 360 to 450 km [8]. To advance the state-of-the-art and enable the synthesis of elemental and mineralogical data at finer spatial

scales, planetary gamma-ray spectrometers with near-HPGe energy resolution, imaging capabilities, high signal-to-noise ratio, high efficiency, low mass, low volume, and no cryogenic cooling are desirable. Large-volume, high resolution 3D CdZnTe (CZT) gamma-ray detectors using pixelated anodes are a suitable candidate to satisfy these requirements.

The wide bandgap (1.6 eV) of CZT, 3D position-sensing, and improvements in low-noise readout electronics and event reconstruction algorithms have enabled CZT detectors to achieve near-HPGe energy resolution at room-temperatures. The 3D position of interactions can be used to correct for electron trapping, material nonuniformity, and weighting potential variation to consistently achieve spectroscopic performance around 0.5% full-width at half maximum (FWHM) at 662 keV for all events. This is comparable to the energy resolution achieved by HPGe used in space applications, which can be on the order of 0.3% FWHM at 662 keV (i.e. for SPI [9] and RHESSI [10]) or even closer to that of CZT (∼0.5% FWHM at 662 keV for MESSENGER [11]). Unlike HPGe, CZT does not require cryogenic cooling, greatly reducing the mass, volume, and risk associated with a payload.

---

* Corresponding author at: University of Michigan, 2355 Bonisteel Blvd, Ann Arbor, MI 48109, USA.
E-mail addresses: abrasara@umich.edu (S. Abraham), zhuyuef@umich.edu (Y. Zhu), snowicki@lanl.gov (S. Nowicki), pbloser@lanl.gov (P. Bloser), hezhong@umich.edu (Z. He).

In space, intense levels of mixed-radiation background can degrade the sensitivity of spectroscopic instruments. The 3D position sensitivity of CZT detectors can help enhance background rejection without an anticoincidence shield. Firstly, the 4-π Compton imaging capability can be used to reject local gamma-ray background from scatter off spacecraft. Secondly, background events due to charged particles can be identified and rejected. While gamma-ray interactions are discrete in interaction positions, charged particles deposit energy starting from one of the out facing surfaces of each CZT detector continuously along their path. The trail of energy deposition due to charged particles will therefore create a spatial signature that can be distinguished from the discrete gamma-ray interactions.

High-resolution large-volume 3D CZT detectors are commercially available and used in many relevant terrestrial applications such as nuclear non-proliferation, defense, medical imaging, and homeland security, but have not yet been used in space applications, putting them at a Technical Readiness Level (TRL) of 4 [12]. CZT has successfully flown in previous space missions such as Swift-BAT [13], AstroSat [14], and NuSTAR [15]; however, the CZT used was much thinner (5 mm or less) and intended for X-ray detection. Virtual Frisch-grid CZT, which can be up to ∼30 mm in thickness but limited in cross-section area, has been proposed for future gamma-ray telescope GECCO [16], but has not yet been space qualified. Compared to 3D CZT detectors using pixelated anodes, virtual Frisch-grid CZT has poorer energy resolution and position resolution for multi-interaction events and will require an anti-coincidence shield to reject background cosmic rays.

High-altitude balloon flight offered a cost-effective avenue to perform a capability demonstration of large-volume 3D CZT detector technology in a space-like environment for the very first time, raising the TRL to 6 for space applications. The relatively small size and weight of CZT instruments made it a candidate for the relatively new hand-launch capability offered by NASA's Columbia Scientific Balloon Facility (CSBF). Compared to traditional small "piggyback" experiments hosted on larger balloon missions, hand-launch payloads are easier to integrate and launch, and suffer from less locally generated background due to the reduced overall mass. The high-altitude balloon flight aimed to show that with minor modifications, current 3D CZT systems can be adapted to operate in near-vacuum space-like environments and detect gamma rays while identifying charged particles to aide in the development of background discrimination algorithms.

2. Payload

2.1. Orion Eagle design

Orion Eagle is a CZT-based imaging gamma-ray spectrometer based on technology developed at the University of Michigan. It contains a single CZT crystal, 20 mm × 20 mm × 15 mm, from Redlen Technologies. It has an array of 11 × 11 anode pixels (1.72 mm pitch) surrounded by a guard ring anode, with a single planar cathode on the opposite side. The energy and position (x,y,z) of radiation interactions in the 3D CZT volume can be determined due to this electrode configuration. The detector design is illustrated in Fig. 1, and the corresponding coordinate system is included. The x–y location is given by the triggered pixel index (pixel size is 1.66 mm × 1.66 mm), and the depth of interaction z is determined by the cathode-to-anode ratio or the electron drift time (interaction-depth resolution is ∼500 μm). The x–y location can be determined on a finer, subpixel scale (resolution of ∼200 μm at 662 keV) if neighboring non-collecting pixel signals are processed as well [17].

The VAD_UM v2.2 application-specific integrated circuit (ASIC), which was developed in collaboration between the University of Michigan and Integrated Detector Electronics AS (IDEAS) [18], was used for signal readout. This ASIC has an adjustable dynamic range and provides digitized pulse waveforms for as many as all electrodes (cathode, 121 anodes, and the guard ring) depending on the selected readout mode.
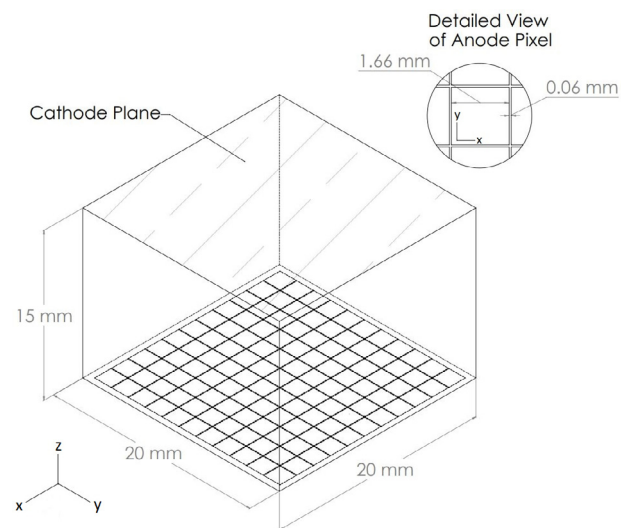

Fig. 1. Drawing of the CZT detector design. A single CZT crystal has an array of 11 × 11 anode pixel electrodes and a planar cathode electrode.

For the balloon flight, the ASIC was operated in trigger-only readout mode with a sampling rate of 40 MHz and the largest available dynamic range setting of 9 MeV. In trigger-only readout mode, only anode pixels with waveforms reaching an adjustable low-energy threshold are read out in addition to the cathode and guard ring anode signals. The minimum low-energy threshold is limited by the electronic noise of the ASIC, which is around 2 keV. However, a conservatively high threshold of 60 keV was chosen for the flight as a precautionary measure in case noise issues arose during the flight. The number of triggered pixels represents the number of anode positions (x–y locations) detecting a significant amount of charge. For gamma ray events, the number of triggered pixels usually describes the number of discrete interactions (i.e. number of locations where a scatter, photoelectric absorption, or pair-production event occurred). Typically, only events involving up to 4 triggered pixels are saved to optimize data storage, as the probability of 5 or more interactions becomes unlikely for most gamma ray events. For interactions that deposit a large amount of energy (greater than a couple MeV), the electron clouds from the interaction may be large enough to trigger multiple pixels [18]. Therefore, for the balloon flight, events with 5 or more triggered pixels were also saved to demonstrate that CZT can measure high-energy charged particle tracks, which may trigger several pixels depending on the incident angle. In this article, events will be referred to by the number of anode pixels triggered (i.e. 1-pixel events for events triggering one anode pixel).

Due to the low-pressure environment expected during the high-altitude balloon flight, Orion Eagle (Fig. 2) has several additional design features not included in previous detector systems designated for in-laboratory or terrestrial use. Primarily, high-voltage design was of utmost importance. During the operation, the cathode of the detector is biased to −3000 V. Pressure changes during ascent/descent and the near-vacuum environment at float altitude are capable of causing high-voltage breakdown in air at small distances as predicted by Paschen's Law [19]. To mitigate risk, the layout of components on the high-voltage generation board and the distribution board were modified and contained in aluminum enclosures. All high-voltage components were potted. The CZT detector was potted with Scotchcast electrical resin 280 (3M) in an aluminum potting dam to provide high-voltage shielding (Fig. 2b). The wire and connectors carrying −3000 V were rated for high-voltage (up to 12 kV) at high-altitude (up to 21 km) (manufactured by Connectronics Corps.). Orion Eagle was tested under −3000 V bias in a small vacuum chamber pumped down to the anticipated float pressure (∼266 Pa) prior to the flight. No issues were observed over six hours of operation at low air pressure.
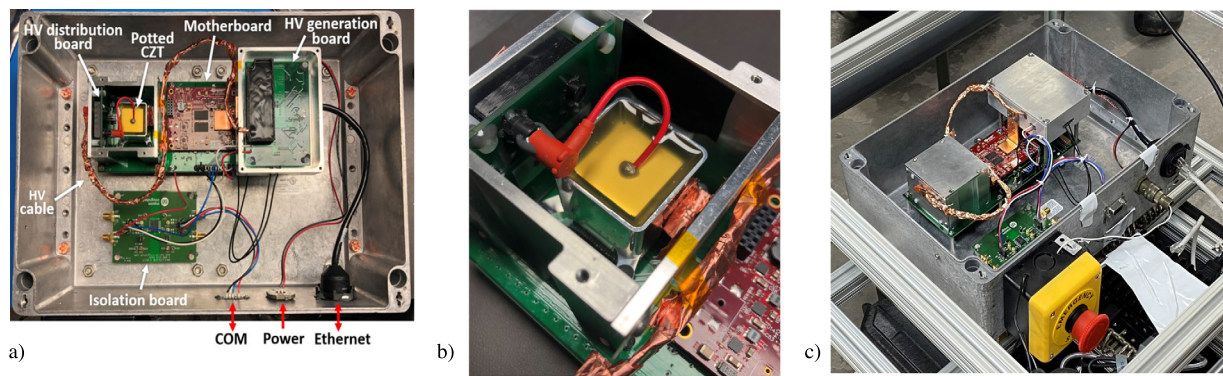
Fig. 2. (a) Orion Eagle hardware with all enclosure lids removed. (b) Potted CZT detector with HV connector attached to the HV distribution board. (c) Orion Eagle with external connectors (emergency stop button, power, ethernet) visible.
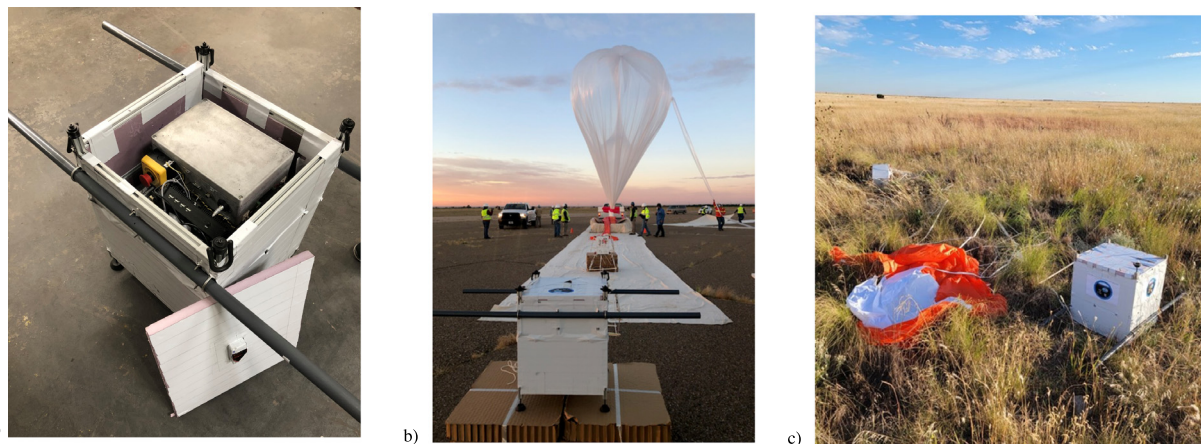

Fig. 3. (a) Orion Eagle (aluminum enclosure) integrated into the gondola with the top insulation lid removed. (b) The payload on the flight-line shortly before launch. (c) The payload upside down after landing, still intact.

Unlike other CZT systems that employ a fan and/or Peltier cooling to maintain room-temperature operation, Orion Eagle has no active temperature regulation to help reduce weight, power consumption, and risk. Copper pieces were used to dissipate heat from the components at greatest risk of overheating: the ASIC and field programmable gate array (FPGA). CZT detectors are capable of operating over a wide range of temperatures, –20 °C to 60 °C [20–23]. Calibration factors (i.e. gain) may drift with changes in temperature, so performing temperature calibrations are needed to help reduce degradation in energy resolution [22].

The top priority of this experiment was to successfully operate CZT in a near-space environment, which meant energy resolution was secondary. Due to limited time and low priority, temperature calibrations were not performed, and an issue with low frequency noise in the cathode signals was not fixed (which prevented the ability to accurately calculate the depth of interaction for 511 keV gamma ray events, so a depth-correction could not be performed). Both of these factors degrade energy resolution even in a laboratory environment. For example, when the CZT detector was tested using a different readout system prior to potting, the depth-corrected energy resolution (FWHM at 662 keV) was 0.42% for single-pixel events, and the energy resolution degraded to 1.16% without depth-correction. Additionally, due to the risk of damage to the detector during the flight and possible harsh landing, only one CZT detector was used, and the detector selected was not one with the best performance nor the largest available size. The best detectors can achieve close to 0.3% FWHM at 662 keV for single-pixel events. It should be noted that future CZT-based detector systems could instead use larger-volume CZT detectors (40 mm × 40 mm × 15 mm) [24] in an array to create an effective area higher than state-of-the-art HPGe used for planetary science missions [25]. The efficiency

of 20 mm × 20 mm × 15 mm CZT is described in detail in Ref. [26], and it is expected that the use of larger-volume single-crystal CZT can help improve efficiency.

2.2. Integration

Orion Eagle is light (5 kg) and easily contained within a 33.2 cm × 23.3 cm × 11.0 cm aluminum enclosure. This enclosure was integrated into a small gondola with an off-the-shelf compact fan-less computer, two external hard drives, and three 29.6 V lithium-polymer batteries. The computer was used to run Orion Eagle's data acquisition software. Raw data (waveforms) was saved on-board via two external memory devices and retrieved after the flight for post-processing. The total power consumption of the whole system was around 20 W, mainly due to the computer and memory devices as Orion Eagle requires only ~4 W. The gondola was 50.8 × 50.8 × 61.0 cm^3 (excluding handles) and had a simple but robust design, as it was intended to be a reusable testbed to hand-launch Los Alamos instrumentation. The gondola fully integrated and with insulation sidewalls taped on is shown in Fig. 3a.

3. High-altitude balloon flight

The Orion Eagle payload (Fig. 3b) was successfully hand-launched at the NASA CSBF facility in Fort Sumner, NM on September 26th, 2021 at 7 am MDT. The float altitude was reached 3.2 h into the flight. During float, the altitude slowly dropped from 38.5 km to 35.4 km. After 5.4 h at float the flight was terminated, and the payload descended back to the ground in 24 min. The flight path is shown in Fig. 4. Stratospheric turnaround conditions caused the balloon to circle
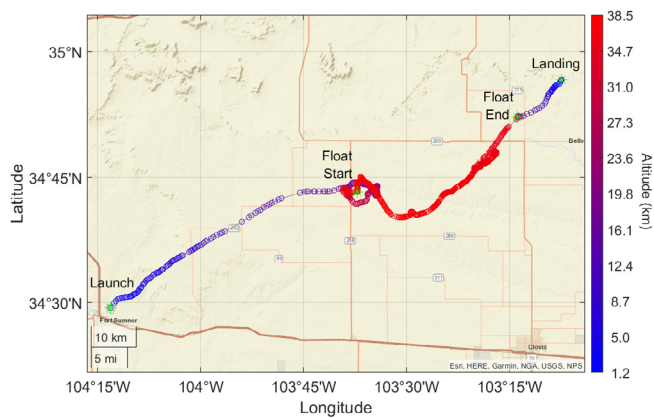
Fig. 4. GPS coordinates provided by CSBF measured during the balloon flight starting in Fort Sumner, NM and ending ~112 km northeast, near the New Mexico-Texas border.

in parts of the flight, which limited the latitudinal/longitudinal distance traveled. The payload landed ~112 km northeast of the launch site in New Mexico near the Texas border (Fig. 4). The temperature and altitude throughout the flight is shown in Fig. 5. All altitudes discussed are relative to sea level. Though the free air temperature reached below –60 °C (measured via CSBF equipment), the temperature sensor on the instrument's ASIC measured between 20 °C and 35 °C during the flight. The ASIC temperature takes time to be impacted by changes in ambient temperature, so it lags behind the free air temperature during the ascent. The ASIC and other electronics generate some heat, which causes the ASIC temperature to reach equilibrium at a temperature greater than the ambient temperature outside the detector enclosure. However, at float altitude, the temperature gradually increased over time instead of reaching an equilibrium. This is likely due to poor heat dissipation caused by the near-vacuum environment (reduced convection). After the descent, the ASIC temperature decreased even though the free air temperature increased, which is likely due to improved heat dissipation.

4. Orion Eagle flight results

4.1. Detector count rate

Orion Eagle was turned on (biased to −3000V) and acquiring data about an hour prior to launch. There was no communication between Orion Eagle and CSBF during the flight. Orion Eagle was equipped to receive a pulse to control the high voltage power and send a return status (via an off-the-shelf isolation board shown in Fig. 2a); however,

this feature was not used to reduce risk. All power successfully remained on until Orion Eagle was manually powered off during recovery of the payload. Orion Eagle was functional with no signs of damage afterwards (Fig. 3c).

The event rate on the day of the flight is shown in Fig. 6. The event rate was averaged over one-minute intervals, and additionally separated by the number of anode pixels triggered during each event. Typically, the ASIC can process thousands of counts per second; thus, the count rates measured during the flight were relatively very low, and the detector dead time is small (<1.5%). The overall detector count rate was steady during the float, only slightly increasing over time, and the maximum count rate was reached during the ascent and descent. The altitude profiles shown in Fig. 7 demonstrate that the change in average count rate during the flight was altitude related. The altitude profiles match the general trend measured in previous balloon flights with radiation detectors [27–29] and generated by atmospheric simulations [30]. The count rate initially increases with altitude, peaks at ~17.5 km (near the Regener–Pfotzer maximum [31]) and then decreases above the peak altitude. This trend is consistent for both the ascent and descent. It should be noted that due to the quick nature of the descent (34 km drop in 24 min), the statistics are sparser. The change of altitude within each minute (over which the event rate is averaged over) may have skewed the first few data points at the beginning of the descent where the drop was fastest.

4.2. Spectroscopy

The anode energy spectrum measured during the flight is shown in Fig. 8. The overall spectrum clearly has a peak at 511 keV, the expected electron–positron annihilation line, and is otherwise a broad continuum with many low energy counts. This energy distribution is similar to observations from other atmospheric gamma ray high-altitude balloon measurements and simulations [29,32–34]. For 1, 2, 3, and 4-pixel events the spectra drop off at sequentially higher energies. For 5-or-more-pixel events, the continuum increases and levels off at high energies likely due to the large energy depositions from heavy charged particles. The peak is easily identifiable and consistently present during the majority of the flight (Fig. 9) indicating the successful operation of the detector. In Fig. 9b, variations in the 511 keV peak centroid over the time of the flight can be seen, likely due to changes in temperature. In the spectrum as a function of altitude measured during the ascent (Fig. 10), the 511 keV peak first becomes discernible just below 10 km.

From a Na-22 calibration measurement prior to the balloon flight, the FWHM of the 511 keV peak for single-pixel events was 6.1 keV (temperature was 28.8 °C ± 1.1 °C). The data was only corrected for channel-by-channel gain variations and had no corrections for temperature or depth-gain variations, which is why the 511 keV peak has poorer energy resolution than normally achieved with 3D CZT in
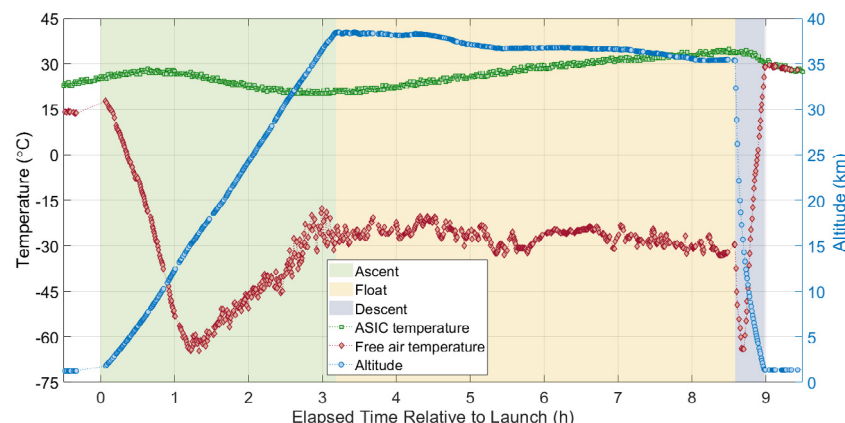

Fig. 5. Conditions during the flight: free air temperature, Orion Eagle ASIC temperature, and altitude. Altitude and free air temperature were provided by CSBF.
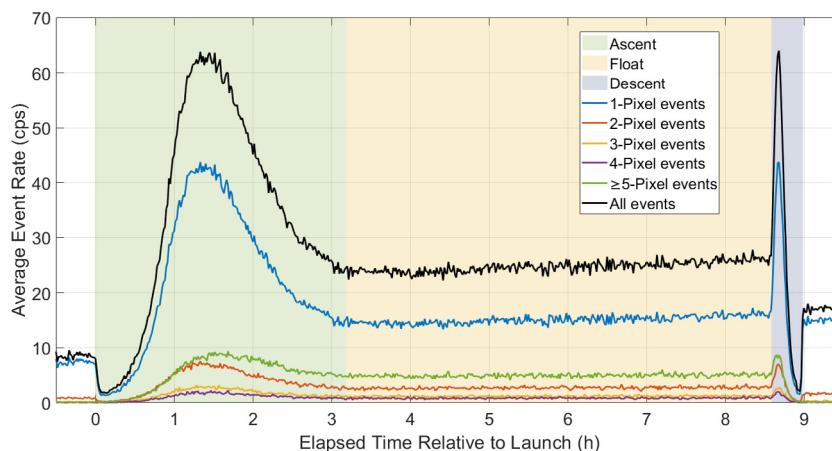
Fig. 6. Average event rate as a function of time relative to the high-altitude balloon launch. The events are categorized by number of pixels triggered.
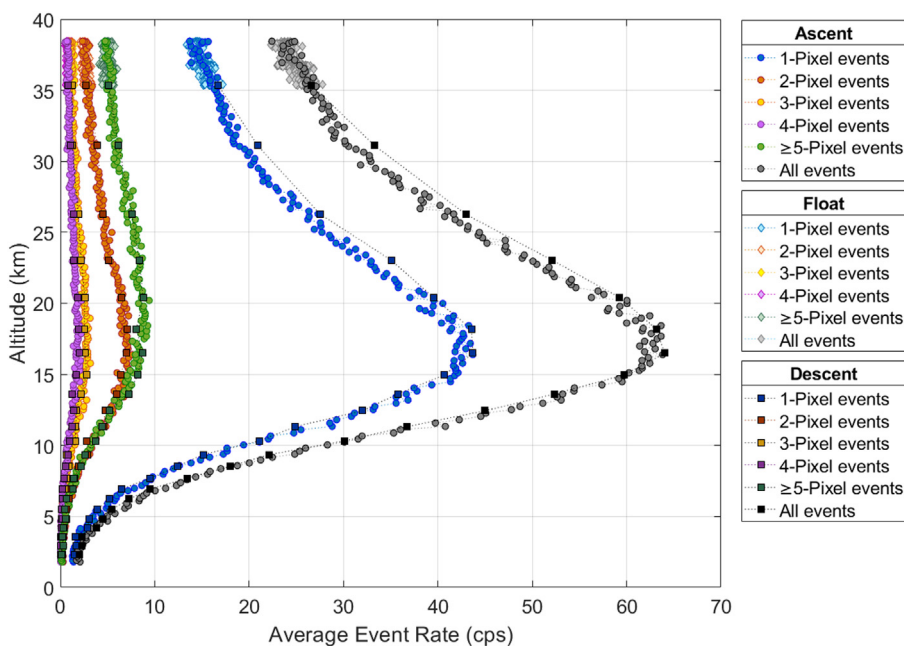

Fig. 7. Altitude profiles of event rate (averaged every minute) for Orion Eagle's ascent (circles), float (diamonds), and descent (squares).

laboratory settings. The 511 keV photopeak measured during the flight (Fig. 8b) was broader, with a FWHM of 11.2 keV for single-pixel events. The broadening of the peak was likely due to a much greater variation in temperature during the flight. In a Na-22 calibration measurement after the flight, the FWHM of the 511 keV peak for single-pixel events was 6.2 keV (temperature was 26.1 °C ± 0.6 °C). The average channel gain was 0.3% greater after the flight. These changes are negligible, especially when considering the difference in temperature during the calibration measurements. This indicates that the detector was not damaged during the flight. If there was damage (either mechanical or radiation-induced), the gain would have significantly decreased. Additionally, no activation peaks were observed during the flight or in post-flight background measurements. Due to the short time frame of the flight, neither radiation damage nor activation were expected based on previous studies [35].

As shown previously in Fig. 5, the temperature ranged from 20 °C to 35 °C during the flight. For an increase in temperature of 15 °C, a decrease in gain of almost ~2% is expected [22,23]. The gain corresponds to the amplitude of the photopeak centroid. For example, if calibration factors determined at 20 °C were applied to data from a

measurement at 35 °C, the reconstructed energy of the 511 keV peak would be underestimated by ~10 keV. If the temperature is stable, the change in gain would have little effect on the FWHM of the peak. However, if the temperature gradually drifts between 20 °C and 35 °C, like in the case of the balloon flight, the peak will be spread over a ~10 keV range if the change in gain is not accounted for. This could be seen in Fig. 9b and in Fig. 11, the distribution of the 511 keV peak during the flight as a function of ASIC temperature. The ASIC temperature is an approximation in this figure: the temperature sensor was not very precise (±0.5 °C error), the temperature was only sampled every minute so values for each radiation event had to be interpolated, and the temperature of the ASIC may not truly reflect the detector temperature when the temperature changes quickly [22]. This approximation and the lack of depth-correction may be the reason for varying spread in the photopeak for different temperature bins. Nevertheless, it is reasonable to conclude that the broadening of the 511 keV peak during the flight was within the error expected due to changes with temperature.

The background event rate after landing was approximately 2 times higher than prior to the launch. The elevated event rate was not observed during the descent, suggesting it is caused by differences
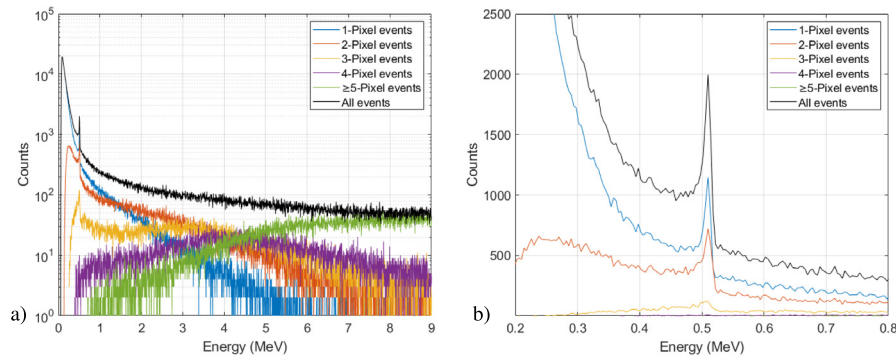
Fig. 8. The anode energy spectra measured during the flight (ascent, float, and descent combined) broken down by event type for (a) the whole dynamic range in log scale and (b) focused on the 511 keV peak on a linear scale.
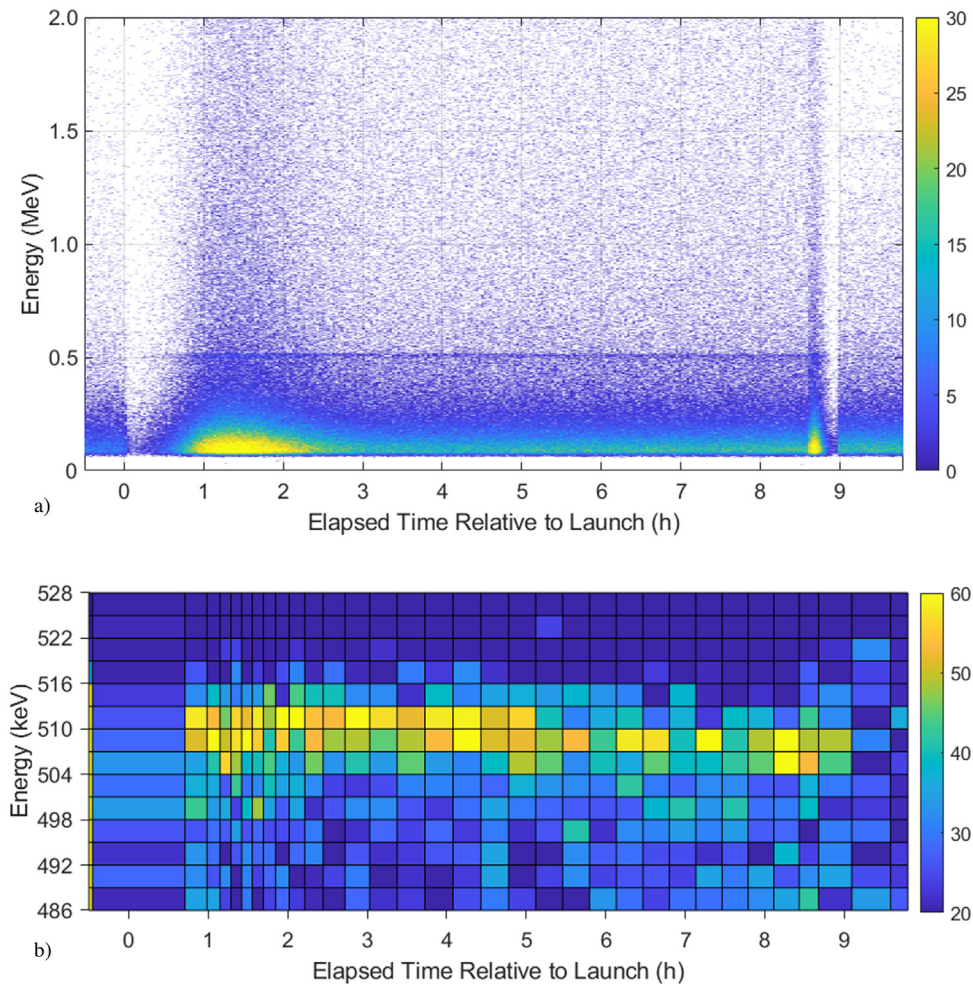

Fig. 9. The anode energy spectrum for all events over time relative to the launch (a) in the range of 0–2 MeV, where each bin is 1 keV by 2 min, and (b) focused on the 511 keV peak where each bin is 3 keV by a variable time bin to compensate for differences in count rate (~30k counts over all energies per time bin). Float altitude was reached at 3.2 h, the descent began at 8.6 h, and the payload landed at 9 h.

in natural background activity and/or the proximity to the ground rather than activation of the payload. Though statistics are poor, the spectrum after landing (Fig. 12) appears to have a peak near 1.46 MeV and a corresponding Compton edge/continuum, which is likely from naturally occurring potassium-40. Prior to the flight, the payload was upright on its legs and hoisted up on cardboard (Fig. 3b), and the detector was near the top of the gondola. After the impact of landing, the payload ended up resting upside down, which places the detector much closer to the ground (Fig. 3c).

4.3. Charged particle detection

During the flight, the majority of events were 1-pixel events, which correspond mainly to low energy gamma-ray interactions (i.e. photoelectric absorption). Charged particles passing perpendicularly through the anode/cathode planes under a single pixel will fall under the 1-pixel event category as well. Charged particles will continuously deposit energy in the detector along their path, essentially creating a line charge. Following the Shockley–Ramo theorem [36], the expected
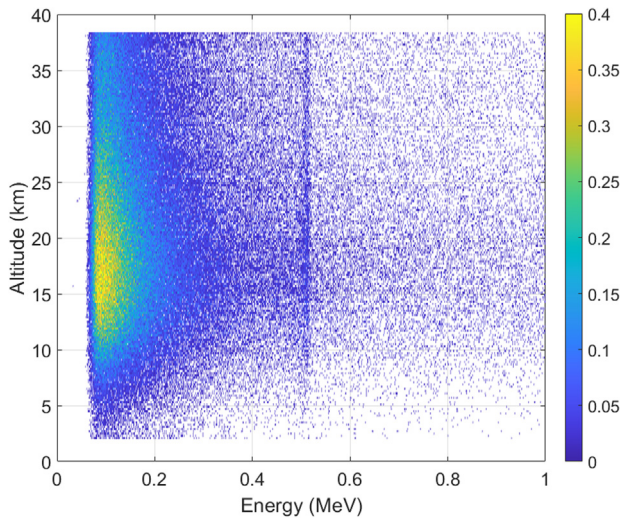
Fig. 10. The anode energy spectrum for all events as a function of altitude measured during the ascent. The color bar gives the counts per second per bin, where each bin is 1 keV by 0.2 km.
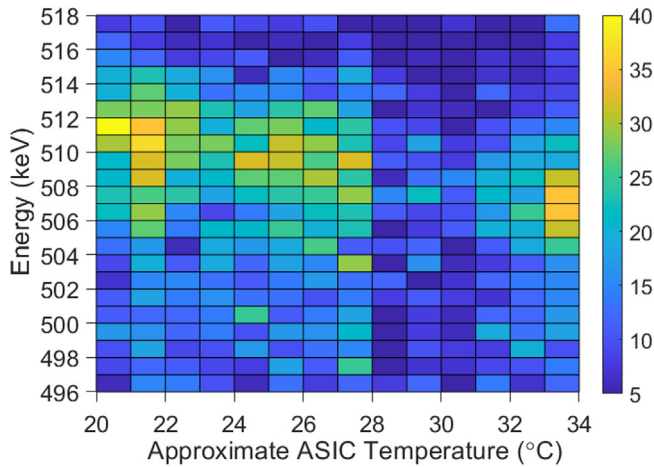

Fig. 11. The distribution of the in-flight 511 keV peak as a function of the approximate ASIC temperature. Each bin is 1 keV by 1 °C.
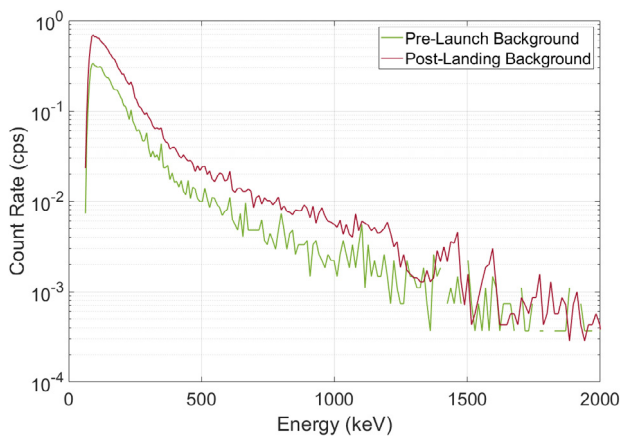

Fig. 12. The 1-P energy spectra measured from background prior to launch at the launch site and after the flight at the landing site.

signal induced from a line charge under a single pixel is different from that of a point charge (i.e. approximation of gamma-ray interaction) in a pixelated detector. Waveforms from Orion Eagle's flight can demonstrate these differences as shown in Fig. 13.

For gamma-ray interactions, the cathode signal will increase linearly as soon as the charge begins to drift, and the anode signal rises very quickly only when the charge is in close proximity to the collecting pixel anode. For gamma-ray interactions in the bulk of the detector (Fig. 13a), the anode signal will rise later than the cathode signal and will have some curvature. The extent of curvature in anode signals depends on the depth of interaction, as it is caused by variation in the anode weighting potential (curve at beginning of signal rise) and the amount of electron trapping/detrapping (rounding at the end of signal rise). For a near-anode gamma-ray interaction (Fig. 13b), the charge begins in close proximity to the collecting pixel so the anode and cathode signals will rise at the same time. Due to the short drift distance, the amount of curvature in the anode signal is limited, and the cathode amplitude will be small relative to the energy deposited.

For a charged particle passing vertically through the detector under a single pixel, the collecting anode signal will increase linearly, the cathode signal will be rounded, and both signals should begin to visibly rise at the same time (Fig. 13c). The slope of the anode signal will be proportional to the energy deposited by the charged particle. An example of a charged particle event with very high energy is shown in Fig. 13d. In this case, the amount of energy deposited is so large that the pre-amplifiers saturate. In the anode channel, this causes the signal to be clipped. For the cathode channel, discharge occurs, causing a rapid decay in the tail of the cathode signal. Events that saturate the anode pre-amplifier are easy to identify due to the high amplitude. Only 1.3% of single-pixel events during the flight caused saturation of the anode signal.

For events that do not saturate the anode pre-amplifier, charged particle events can be identified by abnormally long anode signal rise times, simultaneous rise of anode and cathode signals, and large amplitudes. Differences in signal shapes (i.e. linearity, curvature) can be considered as well. For near-anode gamma-ray events and high energy charged particle events, the timing and shape of anode signals may be similar. In this scenario and for events that saturate the anode pre-amplifier, the cathode amplitude can help classify the events, as the amplitude will be very low for near-anode gamma-ray events, and high for the charged particle events. The differences in characteristics of the cathode and anode signals can be used for discrimination between gamma-rays and charged particles. Table 1 summarizes these characteristics. It should be noted that these are the characteristics expected in an ideal detector system. In practice, the shape of signals can be affected by noise, pre-amplifier settings, poor detector material quality, and non-uniformity in the detector's electric field.

At altitudes above 15 km, 5-or-more-pixel events were the second most probable event type, likely due to the increased presence of charged particles, which are primarily protons [30]. Heavy charged particle interactions incident from most angles will fall under this category. For the 5-or-more-pixel events, the 3D position sensitivity of CZT can be leveraged to visualize charged particles passing through the detector to help separate them from gamma-ray interactions based on differences in spatial signatures. Multiple gamma-ray interactions result in multiple discrete energy depositions, whereas heavy charged particles continuously deposit energy along their path, creating linear ionization tracks. Fig. 14 shows a few examples of linear ionization tracks measured by Orion Eagle. These are rough estimations of the electron cloud distribution, and do not account for weighting potential crosstalk, charge sharing, and local electric field distortions due to large electron clouds. For applications where charged particles are not of interest, events triggering several pixels should not be saved to help reject most charged particles and reduce detector dead time as data size grows large for these events. If charged particles are of interest, the 3D reconstructions of the ionization path could be used to estimate the dE/dx (energy loss per unit path length), which could consequently be used to estimate the energy of the particle if its identity is known.
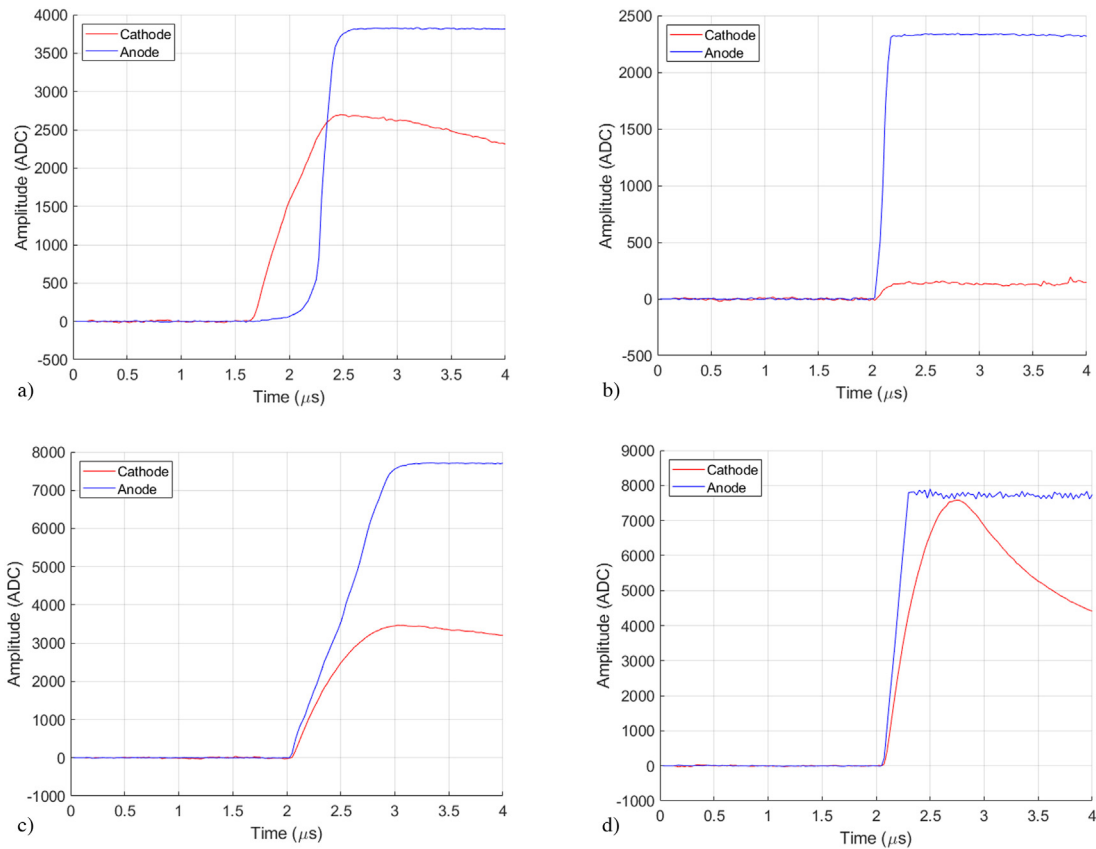
Fig. 13. Examples of waveforms measured during Orion Eagle's flight corresponding to (a) a gamma-ray interaction in the detector bulk, (b) a near-anode gamma-ray interaction, (c) a heavy charged particle interaction, and (d) a heavy charged particle interaction depositing >9 MeV that saturated the anode and cathode pre-amplifiers. Signal decay in the cathode tails in (a) and (c) is due to the cathode pre-amplifier feedback resistance setting whereas in (d) it is due to saturation of the pre-amplifier.
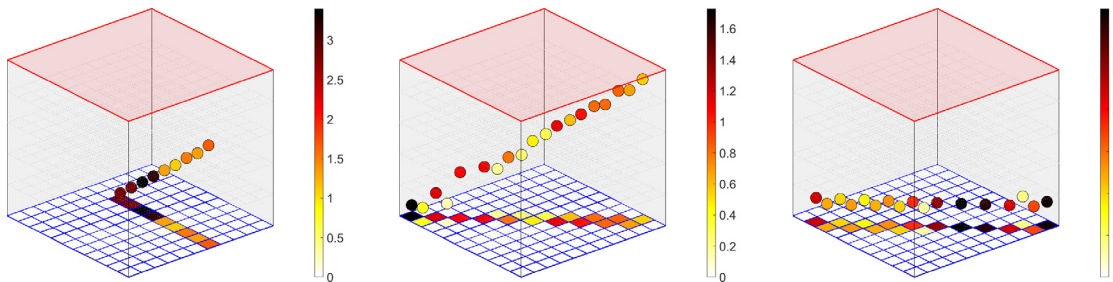

Fig. 14. Visualization of charged particle tracks passing through Orion Eagle's single CZT detector. The red face represents the planar cathode. The 11 × 11 blue grid represents the pixelated anodes, with triggered anodes colored based on the energy deposition. The colored circle markers represent the reconstructed interaction location and energy. The color bar shows the range of the estimated energy deposition per pixel in MeV.

Table 1

Summary of the anode and cathode signal characteristics expected for different interaction types.

Interaction particle type/location	Anode signal			Cathode signal			Relative start time
	Amplitude	Shape	Rise time	Amplitude	Shape	Rise time	
Gamma-ray (in bulk)	*Variable*	*Some curvature*	*Short*	*Variable*	*Linear*	*Variable*	*Cathode rises first*
Gamma-ray(near-anode)	*Variable*	*Minimal curvature*	*Very Short*	*Low*	*Linear*	*Short*	*Both rise at same time*
Charged particle (all depths)	*High*	*Linear*	*Long*	*High*	*Rounded*	*Long*	*Both rise at same time*

5. Conclusions

The high-altitude balloon flight of Orion Eagle demonstrates that 3D CZT detectors can successfully operate in a near-space environment. Modifications to detector design allowed operation in the near-vacuum environment without failure of the high voltage. The detector count rate consistently varied with altitude and peaked at the altitude of the Regener–Pfotzer maximum. The 511 keV electron–positron annihilation line was consistently present as expected, demonstrating the stability of the detector's spectroscopic capability. Cosmic rays were detected, most notably shown by the increase in 5-or-more pixel events at elevated altitudes. The dataset obtained by Orion Eagle was used to visualize the differences in spatial signatures for gamma-rays and charged particles, which can help the development of particle discrimination algorithms.

The successful operation of Orion Eagle and the increase of TRL from 4 to 6 further motivates the use of high-resolution large-volume 3D CZT detectors in space applications.

Declaration of competing interest

Data availability

The authors do not have permission to share data.

Acknowledgments

References

[1] D.J. Lawrence, W.C. Feldman, B.L. Barraclough, A.B. Binder, R.C. Elphic, S. Maurice, D.R. Thomsen, Global elemental maps of the Moon: The Lunar Prospector gamma-ray spectrometer, Science 281 (5382) (1998) 1484–1489.

[2] L.G. Evans, R.C. Reedy, R.D. Starr, K.E. Kerry, W.V. Boynton, Analysis of gamma ray spectra measured by Mars Odyssey, J. Geophys. Res. Planets 111 (E3) (2006).

[3] L.G. Evans, P.N. Peplowski, E.A. Rhodes, D.J. Lawrence, T.J. McCoy, L.R. Nittler, S.C. Solomon, A.L. Sprague, K.R. Stockstill-Cahill, R.D. Starr, S.Z. Weider, W.V. Boynton, D.K. Hamara, J.O. Goldsten, Major-element abundances on the surface of Mercury: Results from the MESSENGER Gamma-Ray Spectrometer, J. Geophys. Res. Planets 117 (E12) (2012).

[4] Y.A. Surkov, F.F. Kirnozov, L.P. Tatsy O.P. Sobornov V.N. Glazov, Uranium, thorium, and potassium in the Venusian rocks at the landing sites of Vega 1 and 2, J. Geophys. Res. Solid Earth 92 (B4) (1987).

[5] P.N. Peplowski, D. Bazell, L.G. Evans, J.O. Goldsten, D.J. Lawrence, L.R. Nittler, Hydrogen and major element concentrations on 433 Eros: Evidence for an L- or LL-chondrite-like surface composition, Meteorit. Planet. Sci. 50 (3) (2015) 353–367.

[6] T.H. Prettyman, N. Yamashita, M.J. Toplis, H.Y. McSween, N. Schörghofer, S. Marchi, E. Ammannito, Extensive water ice within Ceres' aqueously altered regolith: Evidence from nuclear spectroscopy, Science 355 (6320) (2017) 55–59.

[7] T.H. Prettyman, D.W. Mittlefehldt, N. Yamashita, D.J. Lawrence, A.W. Beck, W.C. Feldman, T.J. McCoy, H.Y. McSween, M.J. Toplis, T.N. Titus, P. Tricarico, R.C. Reedy, J.S. Hendricks, O. Forni, L. Le Corre, J.-Y. Li, H. Mizzon, V. Reddy, C.A. Raymond, C.T. Russell, Elemental mapping by dawn reveals exogenic H in Vesta's regolith, Science 338 (2012) 242–246.

[8] W.V. Boynton, W.C. Feldman, I.G. Mitrofanov, L.G. Evans, R.C. Reedy, S.W. Squyres, R. Starr, J.I. Trombka, C. D'Uston, J.R. Arnold, P.A.J. Englert, A.E. Metzger, H. Wänke, J. Brückner, D.M. Drake, C. Shinohara, C. Fellows, D.K. Hamara, K. Harshman, K. Kerry, C. Turner, M. Ward, H. Barthe, K.R. Fuller, S.A. Storms, G.W. Thornton, J.L. Longmire, M.L. Litvak, A.K. Ton'Chev, The Mars Odyssey gamma-ray spectrometer instrument suite, Space Sci. Rev. 110 (1) (2004) 37–83.

[9] J.P. Roques, S. Schanne, A. von Kienlin, J. Knödlseder, R. Briet, L. Bouchet, Ph. Paul, S. Boggs, P. Caraveo, M. Cassé, B. Cordier, R. Diehl, P. Durouchoux, P. Jean, P. Leleux, G. Lichti, P. Mandrou, J. Matteson, F. Sanchez, V. Schönfelder, G. Skinner, A. Strong, B. Teegarden, G. Vedrenne, P. von Ballmoos, C. Wunderer, SPI/INTEGRAL in-flight performance, Astron. Astrophys. 411 (2003) L91–L100.

[10] D.M. Smith, R.P. Lin, P. Turin, D.W. Curtis, J.H. Primbsch, R.D. Campbell, R. Abiad, P. Schroeder, C.P. Cork, E.L. Hull, D.A. Landis, N.W. Madden, D. Malone, R.H. Pehl, T. Raudorf, P. Sangsingkeow, R. Boyle, I.S. Banks, K. Shirey, The RHESSI spectrometer, Sol. Phys. 210 (2002) 33–66.

[11] J.O. Goldsten, E.A. Rhodes, W.V. Boynton, W.C. Feldman, D.J. Lawrence, J.I. Trombka, D.M. Smith, L.G. Evans, J. White, N.W. Madden, P.C. Berg, G.A. Murphy, R.S. Gurnee, K. Strohbehn, B.D. Williams, E.D. Schaefer, C.A. Monaco, C.P. Cork. J. Del Eckels, W.O. Miller, M.T. Burks, L.B. Hagler, S.J. DeTeresa, M.C. Witte, The MESSENGER gamma-ray and neutron spectrometer, Space Sci. Rev. 131 (2007) 339–391.

[12] National Aeronautics and Space Administration, NASA Systems Engineering Handbook (SP-2016-6105), Rev. 2, 2017.

[13] S.D. Barthelmy, et al., The Burst Alert Telescope (BAT) on the SWIFT midex mission, Space Sci. Rev. 120 (2005) 143–164.

[14] V. Bhalerao, et al., The cadmium zinc telluride imager on AstroSat, J. Astrophys. Astron. 38 (31) (2017).

[15] F.A. Harrison, et al., The nuclear spectroscopic telescope array (NuSTAR) high-energy X-ray mission, Astrophys. J. 770 (103) (2013).

[16] A.A. Moiseev, et al., New mission concept: Galactic Explorer with a Coded Aperture Mask Compton Telescope (GECCO), in: 2021 International Cosmic Ray Conference, PoS, ICRC2021, p. 648.

[17] Y. Zhu, S. Anderson, Z. He, Sub-pixel position sensing for pixelated, 3-D position sensitive, wide band-gap, semiconductor, gamma-ray detectors, IEEE Trans. Nucl. Sci. 58 (3) (2011) 1400–1409.

[18] Y. Zhu, Digital Signal Processing Methods for Pixelated 3-D Position Sensitive Room-Temperature Semiconductor Detectors (Ph.D. thesis), University of Michigan, 2012.

[19] F. Paschen, Über die zum Funkenübergang in Luft Wasserstoff Und Kohlensäure Bei Verschiedenen Drücken Erforderliche Potentialdifferenz, Ann. Phys. 273 (5) (1889) 69–96.

[20] Mark Amman, Julie S. Lee, Paul N. Luke, Temperature study of CdZnTe coplanar-grid detectors, IEEE Trans. Nucl. Sci. 53 (5) (2006).

[21] B.W. Sturm, Z. He, T.H. Zurbuchen, P.L. Koehn, Investigation of the asymmetric characteristics and temperature effects of CdZnTe detectors, IEEE Trans. Nucl. Sci. 52 (5) (2005).

[22] J. Xia, Y. Zhu, Z. He, Efficient temperature corrections for gamma-ray energy reconstruction in 3-D position-sensitive CdZnTe detectors, Nucl. Instrum. Methods Phys. Res. A 954 (2020).

[23] S.A. Abraham, Y. Zhu, Z. He, High-temperature operation of 3-D position sensitive CdZnTe detectors, in: Presentation at the 2020 Nuclear Science Symposium and Medical Imaging Conference, 2020.

[24] Y. Zhu, Z. He, Performance of larger-volume $40 \times 40 \times 10$- and $40 \times 40 \times 15$-mm^3 CdZnTe detectors, IEEE Trans. Nucl. Sci. 68 (2) (2021) 250–255.

[25] S.N. Nowicki, Z. He, Y. Zhu, A.M. Parsons, T.H. Prettyman, S.A. Storms, S.A. Wender, Ambient-temperature imaging gamma-ray spectrometer (TIGRS) for high-sensitivity planetary elemental mapping, in: 52nd Lunar and Planetary Science Conference 2021 (LPI Contrib. No. 2548), 2021, p. 1702.

[26] Z. Chen, Y. Zhu, Z. He, Intrinsic photopeak efficiency measurement and simulation for pixelated CdZnTe detector, Nucl. Instrum. Methods Phys. Res. A 980 (2020).

[27] H.V. Neher, Cosmic-ray particles that, J. Geophys. Res. 72 (5) (1967) 1527–1539.

[28] C. Mertens, G. Gronoff, R. Norman, B. Hayes, T. Lusby, T. Straume, W.K. Tobiska, A. Hands, K.A. Ryden, E. Benton, S. Wiley, B. Gersey, R. Wilkins, X. Xu, Cosmic radiation dose measurements from the RaD-X flight campaign: RAD-X FLIGHT DATA, Space Weather 14 (10) (2016).

[29] M. Julien, J.M. Ryan, P.F. Bloser, J.S. Legere, C.M. Bancroft, M.L. McConnell, R.M. Kippen, S. Tornga, Balloon flight results of a fast compton telescope (FACTEL), in: IEEE Nuclear Science Symposium and Medical Imaging Conference Record, 2012, pp. 1893–1900.

[30] F. Lei, S. Clucas, C. Dyer, P. Truscot, An atmospheric radiation model based on response matrices generated by detailed Monte Carlo simulations of Cosmic Ray interactions, IEEE Trans. Nucl. Sci. 51 (6) (2004) 3442–3451.

[31] E. Regener, G. Pfotzer, Vertical intensity of cosmic rays by threefold coincidences in the stratosphere, Nature 136 (1935) 718–719.

[32] J.D. Bowen, M.E. Bandstra, S.E. Boggs, A. Zoglauer, C.B. Wunderer, M.S. Amman, P.N. Luke, Depth dependent background measurements with NCT, in: IEEE Nuclear Science Symposium Conference Record, 2007, pp. 436–444.

[33] C.A. Kierans, S.E. Boggs, A. Zoglauer, A.W. Lowell, C. Sleator, J. Beechert, T.J. Brandt, P. Jean, H. Lazar, J. Roberts, T. Siegert, J.A. Tomsick, P. von Ballmoos, Detection of the 511 keV galactic positron annihilation line with COSI, Astrophys. J. 895 (44) (2020).

[34] A. Akyüz, D. Bhattacharya, K.W. Chuang, D.D. Dixon, T.J. O'Neill, O.T. Tümer, R.S. White, A.D. Zych, Atmospheric gamma rays at geomagnetic latitudes of -29° and +43°, J. Geophys. Res. 102 (A8) (1997) 17, 359–17, 364.

[35] A. Bolotnikov, G. Carini, M. Chekhlov, A. Dellapenna, J. Fried, J. Haupt, S. Herrmann, I. Kotov, D. Medvedev, A. Moiseev, G. Pinaroli, A. Rusek, M. Sasaki, M. Sivertz, L. Smith, E. Yates, Radiation effects induced by the energetic protons in $8 \times 8 \times 32$ mm^3 CdZnTe detectors, Nucl. Instrum. Methods Phys. Res. A 1039 (2022) 166927.

[36] Z. He, Review of the Shockley–Ramo theorem and its application in semiconductor gamma-ray detectors, Nucl. Instrum. Methods Phys. Res. A 463 (1–2) (2001) 250–267.